The Planetary Science Journal, 5:151 (16pp), 2024 June https://doi.org/10.3847/PSJ/ad42a1

Thermodynamic Predictions of Hydrogen Generation during the Serpentinization of Harzburgite with Seawater-derived Brines

Sanjoy M. Som[1,2], Serhat Sevgen[1,3,4], Adam A. Suttle[1,5,6], Jeff S. Bowman[7], and Britney E. Schmidt[8]
[1] Blue Marble Space Institute of Science, Seattle WA, USA; sanjoy@bmsis.org
[2] Space Science and Astrobiology Division, Exobiology Branch, NASA Ames Research Center, Moffett Field CA, USA
[3] Department of Earth, Energy and Environment, University of Calgary, Calgary, AB, Canada
[4] Institute of Marine Sciences, Middle East Technical University, Mersin, Turkey
[5] Engineering & Physical Sciences Research Council, UK Research & Innovation, UK
[6] Department of Materials, The Queen's College, University of Oxford, UK
[7] Integrative Oceanography Division, Scripps Institution of Oceanography, University of California San Diego, La Jolla, CA, USA
[8] Departments of Astronomy and of Earth and Atmospheric Sciences, Cornell University, Ithaca, NY, USA
Received 2023 October 20; revised 2024 April 16; accepted 2024 April 18; published 2024 June 20

Abstract

Salty aqueous solutions (brines) occur on Earth and may be prevalent elsewhere. Serpentinization represents a family of geochemical reactions where the hydration of olivine-rich rocks can release aqueous hydrogen, $H_{2(aq)}$, as a byproduct, and hydrogen is a known basal electron donor for terrestrial biology. While the effects of lithological differences on serpentinization products have been thoroughly investigated, effects focusing on compositional differences of the reacting fluid have received less attention. In this contribution, we investigate how the chemistry of seawater-derived brines affects the generation of biologically available hydrogen resulting from the serpentinization of harzburgite. We numerically investigate the serpentinization of ultramafic rocks at equilibrium with an array of brines at different water activities (a proxy for salt concentration in aqueous fluids and a determinant for habitability) derived from seawater evaporation. Because the existing supersaturation of aqueous calcium carbonate, a contributor to dissolved inorganic carbon (DIC) in natural seawater, cannot be captured in equilibrium calculations, we bookend our calculations by enabling and suppressing carbonate minerals when simulating serpentinization. We find that the extent of DIC supersaturation can provide an important control of hydrogen availability. Increased DIC becomes a major sink for hydrogen by producing formate and associated complexes when the reacting fluids are acidic enough to allow for CO_2. Indeed, $H_{2(aq)}$ reduces $CO_{2(aq)}$ to formate, leading to a hydrogen deficit. These conclusions provide additional insights into the habitability of brine systems, given their potential for serpentinization across diverse planetary bodies such as on Mars and ocean worlds.

Unified Astronomy Thesaurus concepts: Astrobiology (74); Planetary geology (2288)

1. Introduction

Serpentinization is a family of geochemical processes characterized by the aqueous alteration of rocks rich in olivine and pyroxene minerals (e.g., Moody 1976). Serpentinization is also expected on terrestrial planets where rocks and liquid water can interact. Ample evidence suggests that it has occurred, and may continue to occur, on Mars (Ehlmann et al. 2010; McCollom et al. 2022; Tutolo & Tosca 2023), on Jupiter's moon Europa and Saturn's moon Enceladus (Malamud & Prialnik 2013; Glein et al. 2015; Holm et al. 2015), and even on icy moons beyond (Zandanel et al. 2022). Fluids derived from serpentinization are geochemically interesting for many reasons. These reasons include the large pH range of the resulting fluid as a function of reaction temperature (e.g., McCollom & Bach 2009) and the extremely low activities of dissolved silica, making serpentinites the crustal rocks with some of the lowest known silica activities (Frost & Beard 2007).

In this work, we focus mainly on one byproduct of serpentinization: hydrogen as H_2. Everywhere in this contribution, "H_2" and "hydrogen" refer to dissolved hydrogen: $H_{2(aq)}$. This hallmark of serpentinization, the production of hydrogen, is a basal energy source for life and can support chemolithoautotrophy on Earth (e.g., Kelley et al. 2005; Brazelton et al. 2012; McCollom & Seewald 2013; Rempfert et al. 2017; Colman et al. 2022; Howells et al. 2022). Explanations for the variability in hydrogen production during serpentinization have centered on silica activity, temperature, pressure, pH, rock composition (specifically, the iron content of the minerals forming the rock) and water:rock ratio (Frost & Beard 2007; Klein et al. 2009; McCollom & Bach 2009; Klein et al. 2013; Mayhew et al. 2013; McCollom et al. 2016; Leong & Shock 2020; McCollom et al. 2020; Ely et al. 2023), but effects due to salinity have received less attention. Similarly, experimental determinations of olivine dissolution rates (reviewed recently by Oelkers et al. 2018) rarely assess the effects of salinity on hydrogen production variability. We are aware of only the work of Huang et al. (2023), who explore experimentally the effects of salinity on hydrogen production at 300°C (and is discussed below). We thus identify a knowledge gap in understanding hydrogen production when serpentinization is driven by fluids other than freshwater or seawater.

Brines are understood as salty aqueous solutions. Yet, the level of saltiness, quantified as Total Dissolved Solids (TDS), used to identify a solution as a brine, differs between works. Some studies define brines as saltier than drinking water (e.g., Ejeian et al. 2021), while others utilize the much higher threshold of 100 g L^{-1} (Long & Angino 1977), which is saltier than seawater (35 g L^{-1}). Here, we adopt a working definition of brine as an

aqueous solution saltier than seawater (TDS > 35 g L^{-1}). An experimental study conducted by Lamadrid et al. (2017) showed that changing the salinity of the reacting fluid with chloride salts, thus lowering the water activity, slowed the rate of olivine dissolution. Huang et al. (2023) showed experimentally that, at 300°C, salinity can inhibit hydrogen production by increasing the silica activity, which is driven by increased pyroxene dissolution rates. Taken together, such results illustrate that salinity can affect the serpentinization process and may also affect hydrogen production. However, how they translate into thermodynamic predictions is less clear. This further motivates our thermodynamic investigation.

In terrestrial systems, brines are found in contact with rock. The Dead Sea and the Great Salt Lake are some well-known examples. Lesser-known examples include deep-sea hypersaline anoxic basins (DHABs) found so far in the Gulf of Mexico, the Eastern Mediterranean Sea, the Red Sea, and the Black Sea (Antunes et al. 2020; Fisher et al. 2021). Geologic evidence suggests serpentinization driven by brines may have been an active process in the Mediterranean. During the Messinian period, the evaporation of the Mediterranean Sea resulted in brines (Lugli et al. 2015) and ultramafic rocks, as peridotites, exist in the Eastern Mediterranean (Koepke et al. 2002). Indeed, the island of Cyprus contains the Troodos range, which includes the Troodos ophiolite, a formation rich in serpentine (Schuiling 2011).

Brines in contact with rock are likely in many environments on other planets as well. These brines, of varying compositions, may drive similar geochemical reactions. On Mars, in particular, several studies point to brines as responsible for various geochemical and geomorphic processes observed on the surface, from deliquescence to slope linea (e.g., Olsen et al. 2015 and references therein). Motivated by the abundance of olivine detected on the surface (Hamilton et al. 2003), Olsen et al. (2015) investigated experimentally the effects of $MgSO_4$ brines of varying Aw at 25°C on the dissolution rate of forsterite, the magnesium endmember of olivine. While they reported decreased dissolution rates with decreasing Aw, hydrogen production was not reported. Similar to chloride-dominant brines, a thermodynamic investigation has not been undertaken for sulfate-dominant brines. Other planetary examples include water–rock reactions involving brines as suggested by surface deposits on the asteroid Ceres (e.g., Scully et al. 2020) and between ocean brines and the interior silicates on bodies like Europa (e.g., Zolotov & Kargel 2009) and Enceladus (e.g., Glein et al. 2018).

Here, we numerically examine the serpentinization of the ultramafic rock harzburgite by brines of varying compositions derived from seawater evapoconcentration. We focus on harzburgite because it is a common constituent of ophiolitic and abyssal ultramafic rocks on Earth (Bodinier & Godard 2003). We use an array of brines to interrogate via reaction path modeling how changes in concentration (specifically, of dissolved inorganic carbon, DIC, or TCO_2), salinity (as Aw), and pH affect H_2 generation. Pokrovsky & Schott (2000) showed that the activity of CO_3^{2-}, a contributor to DIC, in alkaline solutions at 25°C may inhibit forsterite dissolution, but corresponding measurements of H_2 were not reported.

Our reaction path model and future work investigating the serpentinization of a broader range of brine and rock compositions provide opportunities to understand the effects of brines and their constituents in controlling the generation of biologically available hydrogen released by serpentinization. Examples of future work could include a focus on sulfate-dominated brines (see Liu et al. 2023 for a review) and investigations over broader rock compositions within the ultramafic ternary. This unlocks new assessments to infer the habitability potential of Mars and the ocean worlds of our Solar System where brines are thought to have existed or currently exist (Rivera-Valentin et al. 2020; Buffo et al. 2020; Weiss et al. 2021; McCollom et al. 2022; Zandanel et al. 2022; Castillo-Rogez et al. 2023).

1.1. Seawater-derived brines

In this work, seawater-derived brines are those obtained from the evapoconcentration of seawater. The removal of H_2O molecules from an aqueous system (negative titration) concentrates all the solutes, which affects solution chemistry in different ways. This is functionally equivalent to brines derived from other processes, such as freezing, that can separate a solvent from a solution, but it is technically different from DHAB brines, where seawater is enriched to saturation only by the constituents of the interacting evaporite basement (e.g., halite). Examples of chemical changes that occur during evaporation include complexation, mineral precipitation, and changes in chemical properties such as pH, water activity (Aw), Ionic strength (I), density, and total dissolved salts (e.g., McCaffrey et al. 1987). The advantage of working with seawater-derived brines comes from their existence in, for example, solar salterns, where ponds of different Aw can be sampled near each other and interrogated broadly (e.g., Fisher et al. 2021; Klempay et al. 2021; Paris et al. 2023).

Except for the briniest of solutions derived from seawater evaporation (Aw $< \sim 0.5$), Na^+ and especially Cl^- are the dominant ions (McCaffrey et al. 1987). As evaporation proceeds, the activity coefficient of H^+, γH^+, climbs to 10.07 (25°C) at halite saturation, whereas γOH^- decreases to 0.29 (25°C). Such a change in activity coefficient changes the "effective concentration" of H^+, contributing to the acidification of the water. For example, an initially pure H_2O solution (pH = 7) without any DIC will reach a pH of 6.29 as NaCl(s) is added to halite saturation at 25°C (Figure 1(A)).

Seawater is open to the atmosphere and supersaturated with respect to calcite and aragonite down to several kilometers in the Atlantic and several hundreds of meters in the Pacific (Millero 2009). The presence of magnesium ions (Pytkowicz 1965) and dissolved organic matter (Chave & Suess 1970; Jun et al. 2022) inhibit the growth of solid phases (s) such as $CaCO_3$(s) nuclei. Because $CaCO_3$(s) formation is a source of H^+ via the reaction

$$Ca^{++} + HCO_3^- \leftrightarrows CaCO_3(s) + H^+, \quad (1a)$$

thermodynamic calculations predict more acidic waters than observed when equilibrium with carbonate minerals is considered. The formation of additional carbonate complexes contributes to acidity in fluids with high concentrations of dissolved ions, such as brines. This includes systems rich in magnesium via, for example,

$$Mg^{++} + CO_{2(aq)} + H_2O \leftrightarrows MgHCO_3^+ + H^+. \quad (1b)$$

Because pH is a crucial driver of aqueous chemistry and biochemistry, one should bracket the solution of chemical processes involving seawater, such as evaporation or water: rock reactions as lying in between the two thermodynamic endmembers of carbonate mineral suppression and carbonate mineral equilibrium (Figure 1(B)).

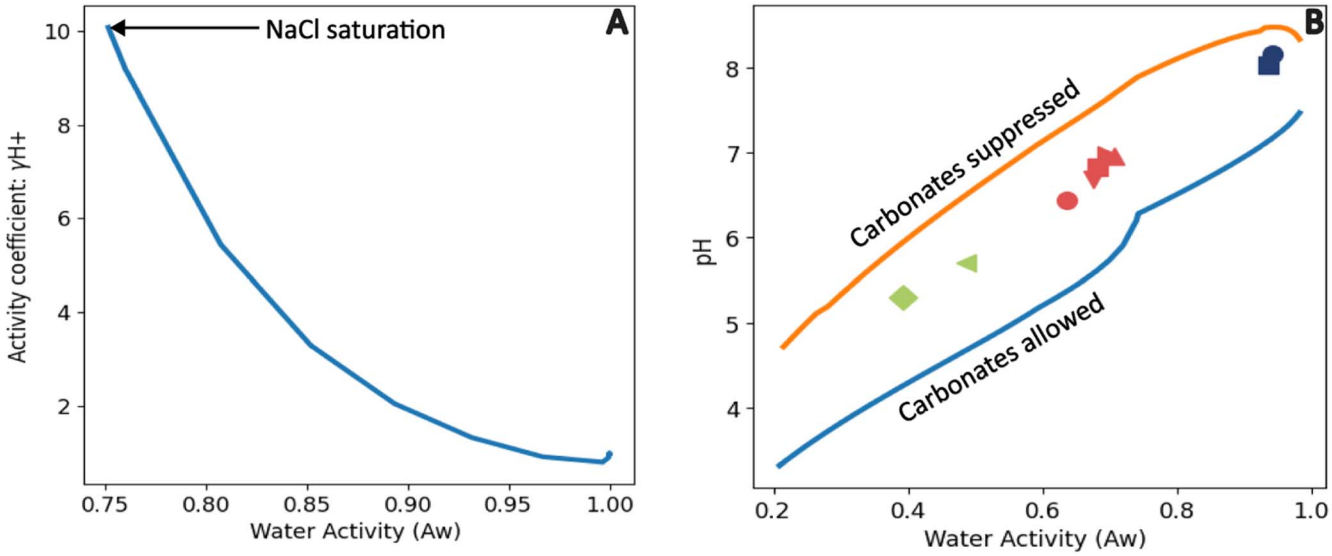

Figure 1. (A): Adding NaCl(s) to pure water at 25°C (no DIC, pH = 7, Aw = 1.0, $\gamma H^+ = 1.0$) until NaCl saturation. (B): Simulations of seawater evaporation at 33°C (Klempay et al. 2021) open to the atmosphere with $pCO_2 = 10^{-3.5}$ bar, with carbonate mineral formation suppressed (top curve) and allowed (bottom curve). Simulations are undertaken under thermodynamic equilibrium. Fluid composition is equivalent to Table 1, except that the pH is set to 8.2. Symbols represent the field data of Klempay et al. (2021), as shown in their Figure (2), and the shapes correspond to different ponds at their sample locality (South Bay Salt Works, San Diego, CA). The blue symbols correspond to ponds at or near seawater salinity, the red symbols correspond to halite-saturated ponds, and the green symbols represent $MgCl_2$-dominated ponds. These field data show some DIC supersaturation since they lie between the two solid lines. All simulations were carried out with the EQ3/6 code. See text for details.

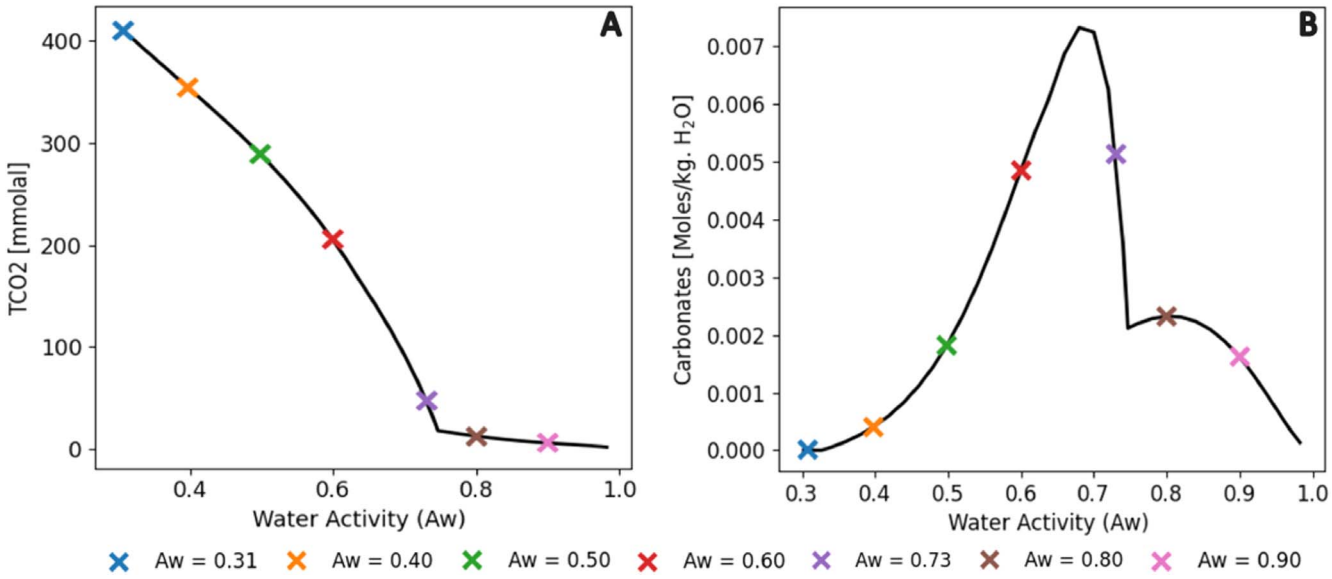

Figure 2. Thermodynamic predictions of seawater evaporation closed to the atmosphere with carbonates allowed to precipitate ($T = 10$°C). (A): Thermodynamic predictions of the total CO_2 (DIC) as seawater is evaporated vs. water activity. (B): Thermodynamic predictions of solid-phase carbonate minerals formed as seawater is evaporated vs. water activity. Evaporation is read from right to left. The crosses represent individual brines selected for this study. The inflections of both curves represent halite saturation (Aw ~0.73).

As evaporation proceeds, the concentration of DIC in the brine increases, and so does the amount of carbonate minerals precipitated when the system is open to an atmosphere containing CO_2. When the system is hypothetically closed to the atmosphere, as the waters get more acidic, the carbonate mineral pool decreases (Figure 2) as carbon transfers from the carbonate pool to the DIC pool via, for example, the dissolution of dolomite, further contributing to the DIC pool:

$$CaMg(CO_3)_2 + 2H^+ \leftrightarrows Mg^{++} + Ca^{++} + 2HCO_{3(aq)}^-. \quad (2)$$

In this work, the starting fluid in all simulated serpentinization reactions is chosen from brines resulting from simulated seawater evaporation closed to the atmosphere in which the formation of solid-phase carbonate minerals is allowed (Figure 2). DIC, speciated into CO_2 due to dropping pH, thus cannot escape to an atmospheric mass. This treatment creates hypothetical fluids with upper-bound fluid DIC designed to magnify effects on hydrogen production and sets up the problem of running a water:rock reaction at 35 MPa where there is no atmospheric mass. Indeed, closing the atmosphere increases the DIC by a factor of 20 for the briniest solutions (400 mmolal compared to 20 mmolal in an evaporative system open to the atmosphere). This 20× increase remains below some natural surface environments, such as soda lakes with

DIC values >2 molal (e.g., Samylina et al. 2014). We assume that our $CO_{2(aq)}$ values speciated from DIC remain below CO_2 saturation for the numerical system pressure under consideration (35 MPa—see Section 2.1).

1.2. Serpentinization

On Earth, serpentinization is a well-documented process observed in different geological settings encompassing a wide range of physicochemical conditions. For example, rocks and fluids resulting from serpentinization have been examined in continental settings such as the Samail ophiolite in Oman (Barnes & O'Neil 1978; Rempfert et al. 2017; Mayhew et al. 2018), the Tekirova ophiolite in Turkey (Hosgormez et al. 2008; Etiope et al. 2011), and the Zambales ophiolite in Philippines (Abrajano et al. 1988, 1990). Serpentinization has also been identified in mid-ocean ridge hydrothermal systems such as the Lost City (Kelley et al. 2001, 2005; Kelley & Shank 2010; Seyfried et al. 2015), Rainbow (Charlou et al. 2002; Douville et al. 2002; Seyfried et al. 2011), Logatchev (Schmidt et al. 2007), Nibelungen (Schmidt et al. 2011), and Von Damm vent fields (McDermott 2015; Grozeva et al. 2020) and possibly below the ice-covered Arctic Ocean (German et al. 2022). Serpentinization has also been documented in subduction zones (Vitale Brovarone et al. 2017, 2020). Chemical energy derived from serpentinization may sustain chemolithoautotrophic microbial communities in the Mariana Trench (Hand et al. 2020).

During serpentinization on Earth, initially oxic and near-neutral waters become reduced and alkaline as the hydration of olivine and pyroxenes proceed to form serpentine group minerals ± magnetite ± brucite ± talc. Hydrogen is mainly generated from the oxidation of Fe^{2+} in olivine and orthopyroxene to Fe^{3+} in magnetite and serpentine through the reduction of water to H_2 (Equation (3)). Because serpentinization is a family of geochemical reactions (see examples in Schulte et al. 2006; Seyfried et al. 2007; Sonzogni et al. 2017; McCollom et al. 2022), serpentinization can be represented generally as

$$\begin{aligned} &x(Mg, Fe)_2SiO_4[\text{olivine}] \\ &\quad + y(Mg, Fe)SiO_3[\text{pyroxene}] + zH_2O[\text{water}] \leftrightarrows \\ &a(Mg, Fe^{+2}, Fe^{+3},)_3Si_2O_5(OH)_4[\text{serpentine}] \\ &\quad + b(Fe^{+2}Fe_2^{+3}O_4)[\text{magnetite}] \\ &\quad + c(Mg, Fe^{+2})(OH)_2[\text{brucite}] + dH_2[\text{hydrogen}], \end{aligned} \quad (3)$$

where the stoichiometric coefficients *a*–*z* of Equation (3), which may be zero, represent the diverse ways serpentinization can be written.

As Equation (3) describes, and while commonly observed, magnetite production (Fe_3O_4) is not strictly necessary. Fe^{3+} can be found distributed in serpentine as well (Seyfried et al. 2007, their Equation (3)). The partitioning of iron into different phases during serpentinization is thus essential for evaluating the production of biologically available hydrogen (Klein et al. 2009, 2013; McCollom et al. 2016; McCollom et al. 2016, 2020, 2022).

Notably, the abiotic production of organic compounds such as formic acid and formate may be prevalent during serpentinization with seawater alongside H_2, but experimental work suggests that their continued reduction to methane is kinetically inhibited (McCollom & Seewald 2001, 2003). As a result, aqueous environments rich in fluids resulting from serpentinization have been prime candidates for examining microbiological processes in energy-poor environments such as the terrestrial subsurface (Sherwood Lollar et al. 2007; Rempfert et al. 2017), the origin and early evolution of life on Earth (Martin & Russell 2007; Russell et al. 2010; Colman et al. 2022), and searching for life in extraterrestrial systems (Schulte et al. 2006; McCollom & Seewald 2013; Holm et al. 2015; McCollom et al. 2022).

Table 1
Initial Fluid Chemistry Representing Terrestrial Seawater ($T = 10°C$)

Starting seawater composition [units of all species except pH: Molality × 10^{-3}]	
pH	7.8*
Na^+	464
Cl^-	546
HCO_3^-	2.3
inc HCO_3^-	2.04
inc $MgHCO_3^+$	0.14
inc CO_3^{2-}	0.038
inc $CO_{2(aq)}$	0.033
inc $Mg(CO_3)_{aq}$	0.026
inc $Ca(CO_3)_{aq}$	0.025
Ca^{2+}	10.2
Mg^{2+}	24.8
K^+	9.8
$SiO_{2(aq)}$	0.16
Fe^{2+}	1.5×10^{-6}
* pH = 7.8 is that of the ocean at depth. Surface water pH is 8.2	
Aw	0.98
I	0.56×10^3

Notes. Seawater is evaporated numerically to create brines of different water activities. The values are taken from McCollom & Bach (2009). Water activity (Aw) and ionic strength (I) are computed based on their values. HCO_3^- (italicized) represents DIC, and "inc" is shorthand for "including."

2. Numerical Methods

2.1. Software Tools and Thermodynamic Databases

EQ3/6 version 8.0a was used to both generate seawater-derived brines and simulate serpentinization reactions. EQ3/6 (Wolery & Jarek 2003; Wolery & Jove-Colon 2004; Wolery 2013) is a suite of codes that encompass both a speciation-solubility code (EQ3NR) as well as a reaction path modeling code (EQ6). The latter solves for the coexisting equilibrium in the fluid between gases, solid minerals, and aqueous species at a given temperature and pressure by using tabulated logK values supplied by the database and using modified Newton–Raphson methods to iterate until the solution converges (Nordstrom et al. 1979; Wolery & Jarek 2003). However, an explicit gas phase in the equilibrium system is not considered. Minerals as solid solutions can be added, which is essential to simulate natural serpentinization reactions (e.g., McCollom & Bach 2009; Klein et al. 2013).

Our starting fluid was terrestrial seawater devoid of oxygen and sulfate, following McCollom & Bach (2009) and Table 1. Initial pH was set to 7.8 (that of seawater at depth), the redox constraint was set to Eh = 0.0V, and electrical charge balance was set on Cl^- as the most abundant ion, such that slight changes imposed on its concentration to maintain a neutral charge would affect the brine composition only minimally. To

Table 2
Select Seawater-derived Numerical Brine Aqueous Compositions Used in This Work (T = 10°C, Carbonate Minerals Are Allowed to Form) Prior to Water:Rock Reaction

Reacting Fluid	Brine #b90	Brine #b73	Brine #b50	Brine #b40	Brine #b31
Aw	0.90	0.73	0.5	0.4	0.31
I	3.08	7.44	13.74	15.93	18.02
pH	5.76	4.38	3.08	2.81	2.43
Na^+	2.48E+00	4.17E+00	3.96E-01	1.59E-01	6.60E-02
K^+	5.23E-02	2.89E-01	4.06E-01	2.71E-01	1.91E-01
Ca^{2+}	5.29E-02	2.96E-01	1.31E+00	1.58E+00	1.82E+00
Mg^{2+}	1.31E-01	7.26E-01	3.20E+00	3.85E+00	4.43E+00
Fe^{2+}	8.01E-09	4.42E-08	1.94E-07	2.33E-07	2.68E-07
Cl^-	2.89E+00	6.46E+00	9.54E+00	1.09E+01	1.23E+01
HCO_3^-	9.06E-03	5.76E-02	2.93E-01	3.56E-01	4.11E-01
inc CO2(aq)	3.25E-03	1.03E-02	3.97E-03	1.23E-03	4.90E-04
inc HCO_3^-	3.26E-03	1.71E-03	1.98E-01	5.84E-05	1.67e-05
inc $MgHCO3^+$	2.55E-03	4.55E-02	2.89E-01	3.55E-01	4.10E-01
$SiO_{2(aq)}$	6.67E-05	3.38E-05	2.06E-05	2.22E-05	2.61E-05
Log γH^+	0.315 5	1.195 5	2.352 3	2.836 6	3.314 2
Log γOH^-	−0.4405	−0.8958	−2.1806	−2.5547	−2.8981

Notes. The initial seawater is that of Table 1. Dissolved ionic species are given in units of molality. HCO_3^- (italicized) represents DIC, and "inc" is shorthand for "including." Aw = water activity, I = Ionic strength. Speciation of these brines will cause mineral precipitation. The resulting aqueous fluid will be at the listed Aw.

create brines, we numerically evaporated seawater by simulating a negative titration of H_2O. As water was removed from solution, the ionic strength of the solution increased beyond $I = 0.1$ molal, where traditional activity coefficient formulations derived from the Debye–Hückel equation lose their applicability, although these formulations are commonly used for seawater where I = 0.7 molal (Wolery & Jarek 2003). For this reason, we used the "ypf" thermodynamic database supplied with EQ3/6 for our evaporation simulations. The ypf database implements the Pitzer equations necessary when working with high ionic strength fluids (e.g., Pitzer 1973; Pitzer et al. 1984; Wolery 1990). Precipitated salts were removed from the system prior to water:rock reaction, to replicate an environmental system where aqueous fluids have been transported away from their source to an unaltered rocky reaction zone.

To simulate water:rock reactions in such a reaction zone, we followed McCollom et al. (2020), who simulated serpentinization reactions with seawater. Their database ("mbn") is designed to simulate reactions from ambient to hydrothermal temperatures (up to 400°C). Like them, we implemented a pressure of 350 bar (35 MPa), which represents pressure conditions for subsurface environments (McCollom & Bach 2009; McCollom et al. 2022) and corresponds to a water depth of 3.5 km on Earth, assuming seawater density of 1025 kg m^{-3}. Additionally, assuming a basalt density of 3000 kg m^{-3}, a pressure of 35 MPa corresponds to a lithospheric depth of 3.1 km on Mars. At that pressure, the solubility (saturation concentration) of $CO_{2(aq)}$ in seawater, $[CO_{2(aq)}]_{sat}$, at 30°C is 1.65 molal and diminishes to 0.79 molal in water at 4 molal NaCl (Aw = 0.83) (Duan & Sun 2003). Increasing water temperature lowers the solubility until ∼100°C, above which the solubility increases (Duan & Sun 2003, their Figure 5). The effects of extreme salinity (>4 molal) on CO_2 solubility at 35 MPa are poorly constrained (Duan & Sun 2003; Spycher & Pruess 2005). As a result, and for simplicity, we assume in this work that $CO_{2(aq)}$ never reaches saturation, given that the highest $CO_{2(aq)}$ we anticipate is on the order of 10^{-2} molal (Table 2). Beyond gas solubility, previous work demonstrated that the thermodynamic properties of the mineral species in serpentinization are relatively insensitive to pressure (McCollom & Bach 2009), so insights gained from modeling are broadly applicable.

The mbn database uses the B-dot formulation of Helgeson (1969), an extended Debye–Hückel equation, to solve for activity coefficients. To our knowledge, no existing Pitzer databases include ultramafic and serpentine minerals. As a result, our water:rock reaction calculations, such as expected aqueous species concentrations in the fluids resulting from serpentinization, should not be taken absolutely. Rather, it is the trends and the comparison of results between brines that are meaningful. We use the "IDEAL OLIVINE" entry in the thermodynamic database as our numerical olivine mineral. "IDEAL OLIVINE," $Fe(Mg)_2SiO_4$, is a solid solution consisting of two endmembers: forsterite, $MgSiO_4$, and fayalite, $FeSiO_4$. We suppress graphite, as well as the Ca-bearing silicate minerals monticellite and andradite (Klein et al. 2013), and we alternatively allow and suppress mineral carbonate formation (specifically calcite, dolomite, magnesite, aragonite, huntite, siderite, hydromagnesite, artinite, and nesquehonite, as they represent all the carbonate minerals in the mbn database) to bracket the solution. Aqueous forms of carbonate, such as $MgCO_{3(aq)}$ and $CaCO_{3(aq)}$, contribute to the DIC pool and are always allowed. We also suppressed the salts carnallite and bischofite in the ypf database, because they do not exist in the mbn database.

Given the difficulties of simulating carbonate supersaturation in natural waters using a thermodynamic equilibrium model, we run the model in two different endmember configurations:

Case 1. Harzburgite is titrated in a brine system containing only a salty fluid where solid-phase carbonates are allowed to form during serpentinization.
Case 2. Harzburgite is titrated in a brine system containing only a salty fluid where solid-phase carbonates are suppressed during serpentinization.

Solid solutions are taken into account in our simulations because the mbn database includes those of serpentine (as chrysotile, greenalite, and cronstedtite), clinopyroxene (as diopside and

hedenbergite), orthopyroxene (as enstatite and ferrosilite), brucite (as Fe^{2+} brucite and Mg brucite), talc (as talc and minnesotaite), and amphibole (as tremolite, pargasite, ferrotremolite, and ferropargasite). Greenalite, $Fe_3Si_2O_5(OH)_4$, is the Fe^{2+} bearing serpentine endmember. However, cronstedtite allows for the substitution of ferric iron into the serpentine mineral structure, $Fe_2^{2+}Fe_2^{3+}SiO_5(OH)_4$, as well. Working with cronstedtite creates new opportunities to better track iron oxidation pathways in serpentine for hydrogen production as the water–rock reactions proceed (Klein et al. 2013 and below). We suppressed antigorite, a polymorph of Mg-bearing serpentine mineral found mostly common in high-pressure tectonic settings (e.g., subduction zones; see Vitale Brovarone et al. 2017) and replaced it with chrysotile as the representative Mg endmember of serpentine minerals in shallow subsurface environments like ocean floors and ophiolites (Evans et al. 2013; McCollom et al. 2022). Lizardite was omitted because it is also a magnesium endmember of serpentine and has very similar thermodynamic properties to chrysotile (Evans 2004).

2.2. Brine Formation Procedure

Water activity (Aw) was selected as the proxy for salinity, due to our interest in connecting brine chemistry with biological habitability (Klempay et al. 2021; Paris et al. 2023). Water activity provides, in a single parameter, an estimate of the water available for biology. Indeed, Aw exerts a strong control over fungal germination and microbial metabolism. Fungal germination has been measured at Aw as low as 0.585 (Stevenson et al. 2017), and microbial metabolism has been projected to occur down to Aw = 0.540 (Paris et al. 2023). Given that hydrogen resulting from serpentinization could be transported beyond the rocky reaction zone and we expect the water activity to change as the serpentinization reaction proceeds, solutions saltier than the limit of life were studied as well.

To get a suite of brines with broad chemical variability (down to Aw = 0.31), we focused on evapoconcentration as the brine-creation process. Modeling was initiated by first speciating seawater at 10°C using EQ3NR. The resulting fluid was then evaporated with EQ6 by removing 55.2 moles of H_2O while keeping track of evolving fluid composition. Full evaporation would entail removing 55.55 moles H_2O. Removing more than 55.2 moles of H_2O caused numerical instabilities. Results from seawater evaporation described a relationship between reaction progress ξ ("xi" in the output files) and Aw. This relationship was used to obtain ξ^* for an Aw of interest by linear interpolation, where $\xi^* < 1$. The brine was rescaled such that another evaporation simulation interrupted at $\xi = \xi^*$ would have a solvent mass of 1 kg. This kept the initial water:rock ratio close to unity for serpentinization modeling. Select compositions of brines with different Aw obtained from these simulations are tabulated in Table 2.

2.3. Serpentinization Procedure

Brines were reacted with harzburgite. While acknowledging that peridotite composition strongly controls hydrogen production (Ely et al. 2023), we nonetheless limited ourselves to a single harzburgite composition and used one described in Klein et al. (2013) consisting of 80 wt% of Fo90 olivine, 10 wt% of orthopyroxene (90% enstatite and 10% ferrosilite), and 10 wt% of clinopyroxene (90% diopside and 10% hedenbergite), where the percentages of endmember minerals in each solid solution are mole fractions. We focused on a single composition because harzburgite compositions are by far the dominant peridotite composition on Earth (Bodinier & Godard 2003) and because our aim in this contribution is focused on the effects of reacting fluid chemistry.

Because EQ3/6 is an equilibrium code, reaction kinetics cannot be explicitly considered. However, because the reduction of CO_2 to CH_4 can be kinetically inhibited in natural serpentinizing systems (McCollom & Seewald 2001, 2003; McCollom 2016), methane and methanol were additionally suppressed. Peridotite was titrated into each brine until 1 kg of rock was equilibrated with 1 kg of starting fluid at 10°C. Then the whole system was heated to 400°C. EQ6 book-kept the chemistry of the whole system in discrete steps as the reaction progress ξ advanced from 0 ($T = 10$°C in our case) to 1 ($T = 400$°C in our case).

2.4. Expected Hydrogen Produced from Fe^{3+} Mineralogy

Hydrogen is generated from the oxidation of ferrous iron to ferric iron (Equation (3)). Therefore, accounting for all the ferric iron in the resulting mineralogy can give a proxy for the amount of hydrogen (per mole olivine reacted) generated. We follow the methods of McCollom et al. (2022) to compute the hydrogen produced by the two minerals where Fe^{3+} reside: $(Mg,Fe)_3Si_2O_5(OH)_4$ (serpentine) Fe_3O_4 (magnetite)

$$H_2^{serp}\text{generated per mole olivine} = 3 \times (\text{Moles}^{serp}) \times (1 - \text{Mg}\#^{serp}) \times (Fe^{3+}/Fe_{total})^{serp} \times 0.5/\text{Moles}^{olivine}$$

with $(Fe^{3+}/Fe_{total})^{serp} \sim 2^*\text{Moles}^{cronstedtite} / (3^*\text{Moles}^{greenalite} + 4^*\text{Moles}^{cronstedtite})$, keeping in mind that there are three moles Fe^{3+} per mole serpentine and that it takes the creation of two moles of Fe^{3+} to liberate one mole of H_2 ($2Fe^{2+}O + H_2O \leftrightharpoons Fe_2^{3+}O_3 + H_2$).

Also,

$$H_2^{magnetite}\text{generated per mole olivine} = (\text{Moles}^{magnetite})/\text{Moles}^{olivine},$$

so then

$$H_2 \text{ generated} = H_2^{serp} + H_2^{magnetite}. \quad (4)$$

For ease of reproducibility of our results, we have developed Python wrapper scripts around EQ3/6 that we collectively called chEQWRk ("check work") to automate the processing described above. Those scripts (Som et al. 2024) are available on the Astrobiology and Habitable Environments database (AHED).[9] GitHub contains dynamic versions of chEQWRk,[10] and a specific version that supports this work.[11] ChEQWRk is designed to run in a Linux environment. We performed our calculations on a standard laptop computer running EQ3/6 on Ubuntu Linux 18.04 LTS as WSL2 within Windows 11.

3. Results

3.1. Hydrogen Production and pH

Thermodynamic predictions of hydrogen concentration following the alteration of harzburgite with different seawater-derived brines as a function of temperature are shown in Figure 3. For fluids with Aw >0.8, far from NaCl saturation,

[9] https://ahed.nasa.gov/
[10] https://github.com/sanjoymsom/chEQWRk
[11] https://github.com/sanjoymsom/chEQWRk/releases/tag/v0.1.1

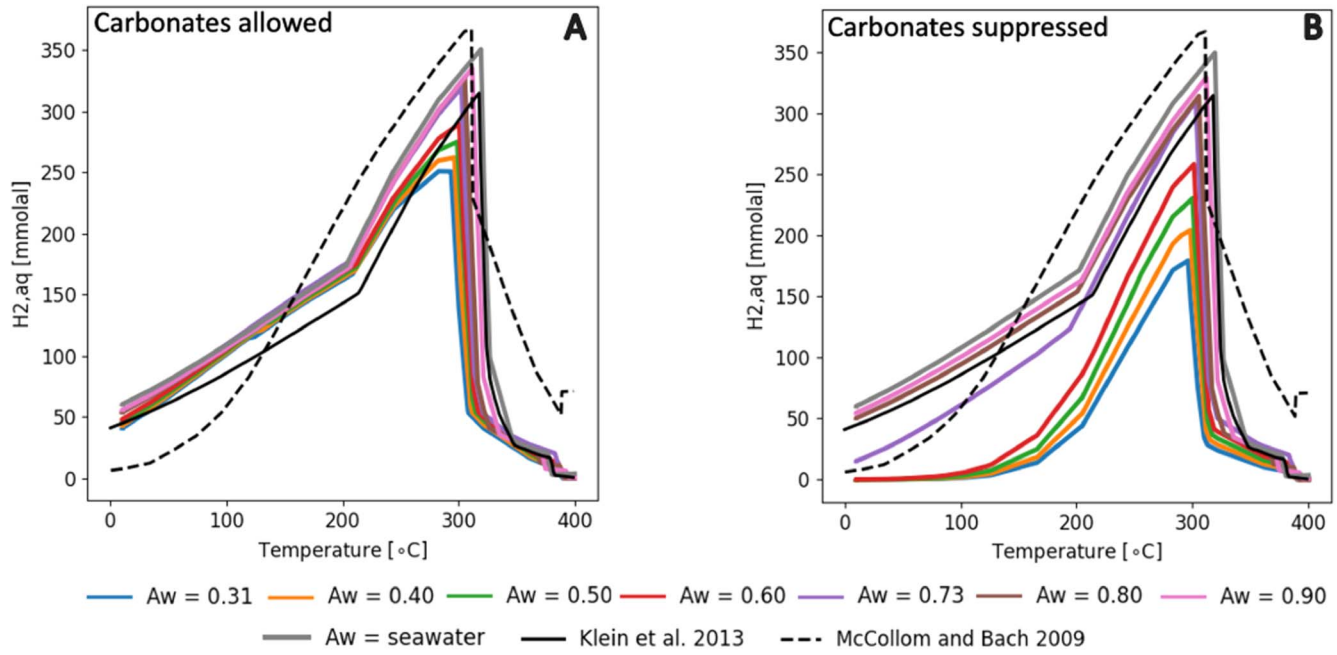

Figure 3. Hydrogen in seawater-derived brines resulting from the serpentinization of distinct brine compositions of varying Aw as a function of temperature at 350 bar (35 Mpa) and a water:rock ratio equal to 1. (A): Carbonates allowed. (B): Carbonates suppressed.

H_2 concentrations are only marginally affected by changes in apparent salinity over the full temperature range. This remains true for both cases investigated: when carbonates are allowed to precipitate and are in thermodynamic equilibrium with the aqueous fluid (Figure 3(A)), reacting fluid water activity and DIC content do not affect H_2 production at temperatures less than ~200°C. The largest differences are observed at reaction temperatures between ~210°C and ~300°C, where H_2 production from the saltiest brines (Aw = 0.31) is about a third below that of seawater (250 mmolal vs 350 mmolal) at peak H_2 production. Peak H_2 production also shifts toward colder temperatures as fluid Aw decreases (318°C for seawater versus 291°C for the saltiest brine studied).

In contrast, when carbonates are prevented from precipitating (as done in Klein et al. 2013), effectively representing complete carbonate supersaturation, H_2 production decreases significantly at Aw greater than NaCl saturation (Figure 3(B)). H_2 production for fluids with Aw < 0.6 is effectively inhibited below 100°C. At peak H_2 production, the saltiest brines produce half the H_2 compared to seawater (177 mmolal versus 350 mmolal). Supersaturation of carbonates does not create differences in the observed temperature shift of peak H_2 production compared with carbonate mineral equilibrium.

The pH of the resulting fluid is also sensitive to the pH of the starting fluid (Table 2) but not to the degree of carbonate supersaturation (Figure 4). This is because the formation of *aqueous* calcium carbonate from Ca^{++} and HCO_3^- releases H^+ in the same way as the formation of *solid* calcium carbonate from Ca^{++} and HCO_3^- releases H^+ (Equation (1)). For brines with Aw >0.80, hyperalkaline fluids are expected at $T = 10$°C. For all other brines at 10°C, $8 < pH < 10$. The pH steadily decreases as temperature increases. Acidic conditions are encountered at $T > 122$°C when the reacting fluid is a seawater-derived brine of Aw < 0.6, $T \sim 200$°C at halite saturation, and $T > 375$°C with reacting fluids of Aw >0.8.

3.2. Mineralogy

Thermodynamic predictions of stable mineralogical assemblages following the alteration of peridotite with different seawater-derived brines as a function of temperature are shown in Figure 5. As the Aw of the starting fluid decreases, the thermodynamic stability of olivine is pushed toward lower temperatures. With seawater as the reacting fluid, olivine is stable at alteration temperatures above 320°C, whereas if a seawater-derived brine of Aw = 0.31 is the reacting fluid, olivine can remain stable at temperatures as low as 300°C. Magnetite is also stable at low temperatures when brines are the reacting fluid.

3.3. Iron Oxidation State

The production of hydrogen is linked to the oxidation of Fe^{2+} to Fe^{3+}. Predictions of hydrogen generated based solely on the Fe^{3+} present in serpentine and magnetite are shown in Figure 6. When carbonates are suppressed, effectively simulating fluid supersaturated in DIC, the stability of magnetite at low temperatures and low Aw translates into expected H_2 production (Figure 6(B)). This stands in contrast with there being very little thermodynamically predicted H_2 production (Figure 3(B)) and points to a low-temperature hydrogen sink when carbonate supersaturation exists rather than H_2 formation inhibition. In these same conditions of supersaturation, serpentine, alongside magnetite, is also a reservoir of Fe^{3+}, as illustrated in Figure 7(B). There, the ratio $Fe^{3+}/(Fe^{2+} + Fe^{3+})$ of serpentine as a function of temperature and water activity is threefold higher with brines of Aw < NaCl (s) saturation. The Mg# of olivine, brucite, and serpentine are illustrated in Figures 8(A)–(F). Grouped together, these calculations compare well with the results shown in Figures 6 and 7 of Klein et al. (2013), who focused on seawater as the primary reacting fluid.

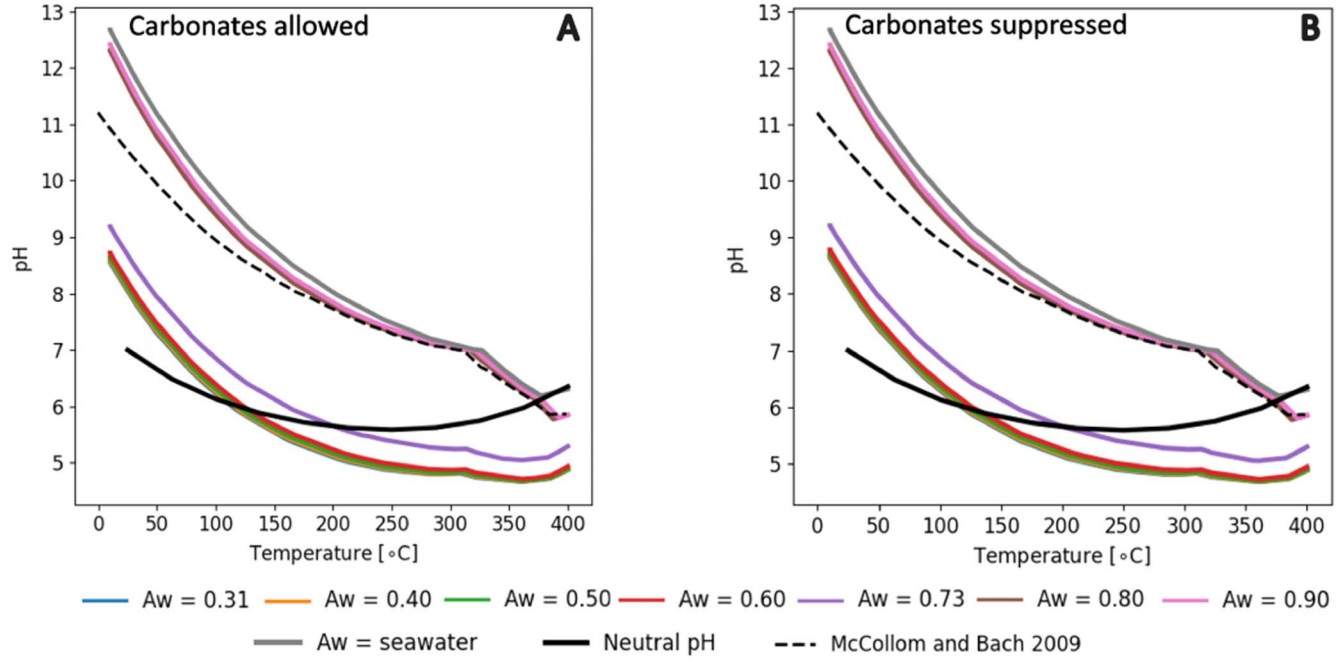

Figure 4. pH in seawater-derived brines resulting from the serpentinization of distinct brine compositions of varying Aw as a function of temperature at 350 bar (35 MPa) and a water:rock ratio equal to 1. The plots are identical, indicating that the carbonate saturation level does not measurably influence the pH in these water:rock systems. Rather, it is the rock composition that is the primary driver of serpentinized fluid pH. (A): Carbonates allowed. (B): Carbonates suppressed.

3.4. Water Activity

The water activity of the reacting fluid does not remain constant during serpentinization reactions. In this investigation, starting fluids were aqueous brines removed from their equilibrium mineralogical assemblage. Calculations show that exposure of these fluids to new rock apparently causes a significant shift in water activity (but see Discussion). For example, the serpentinized fluid resulting from the saltiest starting brine (Aw = 0.31) having reacted with harzburgite results in an Aw of 0.67 at equilibrium (Figure 9, $T = 10^{\circ}$C), regardless of the state of carbonate supersaturation. Aqueous fluids of Aw = 0.67 and above are conducive to life (Stevenson et al. 2017; Paris et al. 2023). As reaction temperature increases, Aw decreases slightly for brines with Aw less than halite saturation up to 50°C. As reaction temperatures rise above 50°C, Aw increases monotonically such that, at 400°C, all fluids have Aw >0.85.

4. Discussion

In terrestrial environments, alkaline fluids and elevated hydrogen concentrations resulting from low-temperature serpentinization by seawater are observed and well understood (e.g., Palandri & Reed 2004). Hydrogen is generated by the oxidation of liberated ferrous iron originally in the protolith by water (Equation (3)), and the alkaline character (as $[OH^-]$) comes dominantly from the absence of Ca-OH minerals at low temperatures, resulting in fluids rich in Ca^{2+} and OH^-, termed "type 2" waters by Barnes & O'Neil (1969). An increase in salinity (a decrease in water activity) causes the pH to decrease (Figure 1(B)) due to both the increase in the activity coefficient of H^+ as a function of salinity and because of the complexation of carbonate and bicarbonate anions with cations of high activity, liberating H^+ (e.g., Equations (1a) and (1b)). This increase in acidity can transfer the solid carbonate pool to the dissolved inorganic carbon (DIC) pool (Figure 2), and due to the pH-dependent speciation of DIC (e.g., Andersen 1996 p.183), the proportion of DIC speciating to aqueous CO_2 increases as pH decreases as well. Aqueous CO_2 is a sink for H_2 produced by serpentinization via reduction to formate (For = $HCOO^-$) and formic acid (HCOOH) given the kinetic inhibition of methane (CH_4):

$$CO_2 + H_2 \leftrightarrows For + H^+, \tag{5a}$$

$$For + H^+ \leftrightarrows HCOOH. \tag{5b}$$

In brines with Aw $< \sim$0.9, $MgHCO_3^+$ dominates the DIC pool (Table 2). This pool acts as a source of $CO_{2(aq)}$. Indeed, as $CO_{2(aq)}$ is consumed by Equation (5a), more is formed by Equation (1b). Where exactly the equilibrium resides is sensitive to reaction temperature, pH, and oxidation state (e.g., McCollom & Seewald 2003, their Figure 1). McCollom & Seewald (2003) show that formate abundance is dominant over formic acid at pH greater than ~4 (175°C) and ~5 (250°C) for a fixed hydrogen concentration at 35 MPa, with formate increasing in abundance as H_2 is increased.

In saline systems, the equilibrium of formate is complicated by the existence of formate complexes. Here, we define

$$\begin{aligned}\text{Total formate} \;=\; & For + Mg(For)^+ + Mg(For)_{2(aq)} \\ & + Na(For)_{(aq)} + Fe(For)^+ + Fe(For)_{2(aq)}.\end{aligned} \tag{6}$$

We show an overabundance of total formate over formic acid across the chemical state of our study (Figures 10(A) and (B)). That H_2 is being consumed is supported by comparing Figure 3(B) with Figure 6(B). Together, the differences between these plots point to an H_2 sink as the additional control on H_2 availability. Indeed, Figure 6(B) shows that abundant H_2 should be expected at $T < 200^{\circ}$C, given the formation of magnetite and serpentine, but H_2 is depressed (Figure 3(B)). Comparing these figures with Figure 10(B)

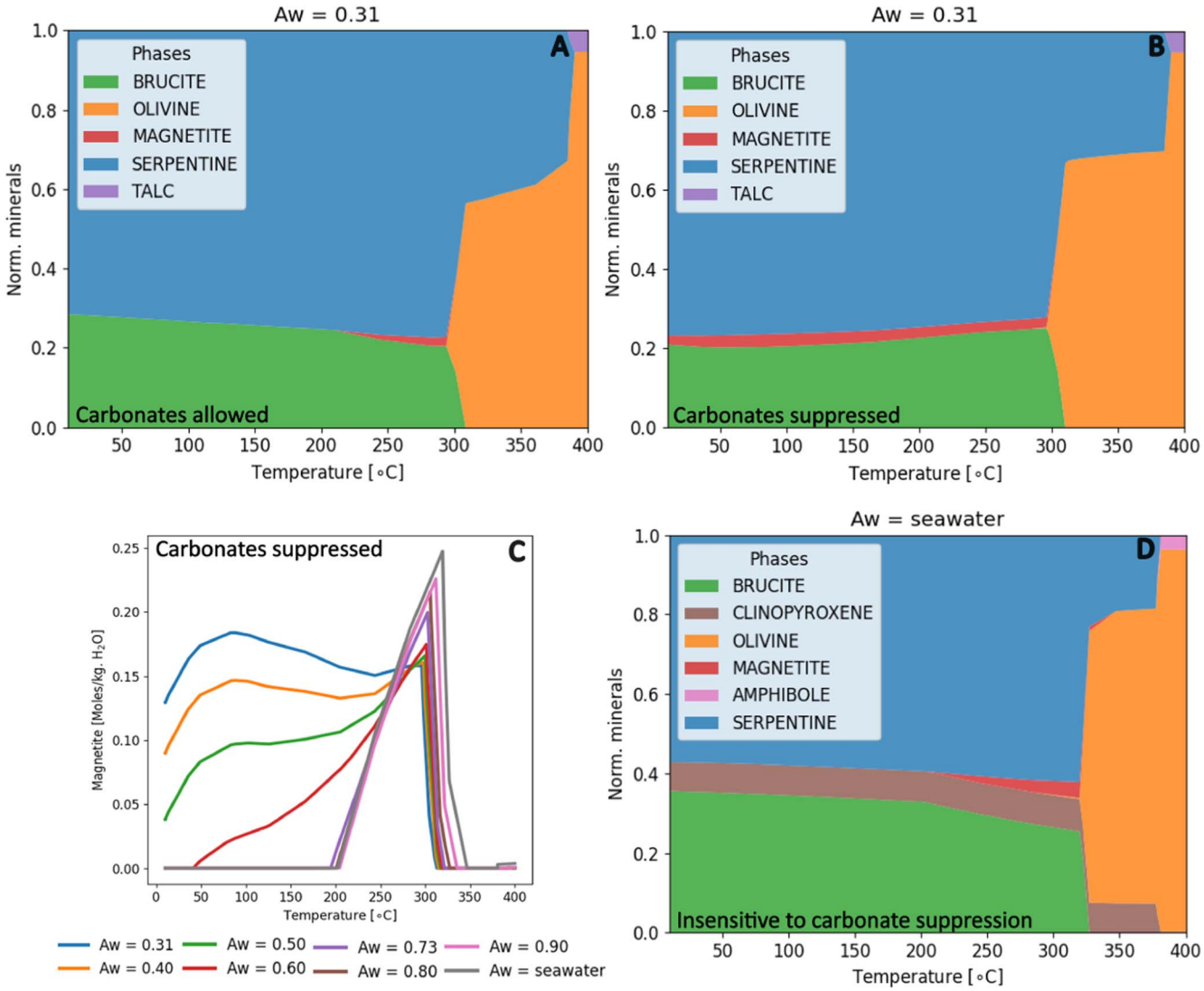

Figure 5. Alteration mineralogy (mole normalized). (A): Starting fluid Aw = 0.31; mineral carbonates are allowed to precipitate during serpentinization but are omitted here for comparative clarity with panel (B). (B): Starting fluid Aw = 0.31; mineral carbonate formation is suppressed during serpentinization. Magnetite is stable to low temperatures. (C): Magnetite formation for starting fluids of different Aw; mineral carbonate formation is suppressed. (D): Expected alteration mineralogy for seawater as the starting fluid, regardless of carbonate suppression option. See Section 2 for a description of the reacting minerals.

shows that the total formate is the sink. Similar amounts of expected H_2 produced below ~150°C (between 250 and 300 mmolal; Figure 6(B)) are found as total formate instead (Figure 10(B)).

Calculations show that carbonate supersaturation at 10°C causes a 30× increase in total formate concentration compared to carbonate equilibrium (Figures 10(A) and (B)). As a result, it is the thermodynamic stability of total formate in fluids resulting from serpentinization with DIC-rich brines, as shown in Equations (5) and (6), that is the important control on hydrogen concentrations in the systems studied here, complementing similar conclusions based on kinetic and experimental work at high temperature (200°C) by Jones et al. (2010), who reported diminished H_2 due to Fe^{++} incorporation into carbonates in DIC-rich fluids.

We predict that the mineralogy resulting from the serpentinization of harzburgite with low-Aw and high-DIC brines accumulates less brucite compared to mineralogy resulting from regular seawater serpentinization (Figure 5). This is important because brucite plays a significant role as a repository for iron, specifically Fe^{2+}, during the process of serpentinization (Templeton & Ellison 2020) and hydrogen production is tightly coupled to the oxidation of ferrous iron. In general, the formation of brucite is attributed to the limited availability of the required SiO_2 in olivine; therefore, brucite is more likely to be found in olivine-rich rocks with low silica activity, such as dunites (an olivine-rich peridotite) (e.g., Klein et al. 2013). During the hydration of peridotite, the formation of serpentine instead of brucite can be influenced by reactions involving pyroxene minerals, because of their impact on SiO_2 activity (Templeton & Ellison 2020). However, during the hydration of harzburgites, the equilibrium between olivine and brucite can still be established (Klein et al. 2009, 2013), and brucite can also accumulate at low temperatures due to the rapid alteration of olivine compared to pyroxene (Alt et al. 2007; Templeton & Ellison 2020). Indeed, at lower temperatures (<200°C), brucite can retain more ferrous iron and prevent Fe^{2+} from oxidizing into Fe^{3+} within magnetite and serpentine (Seyfried et al. 2007; McCollom & Bach 2009; Klein et al. 2013). Consequently, the presence of brucite

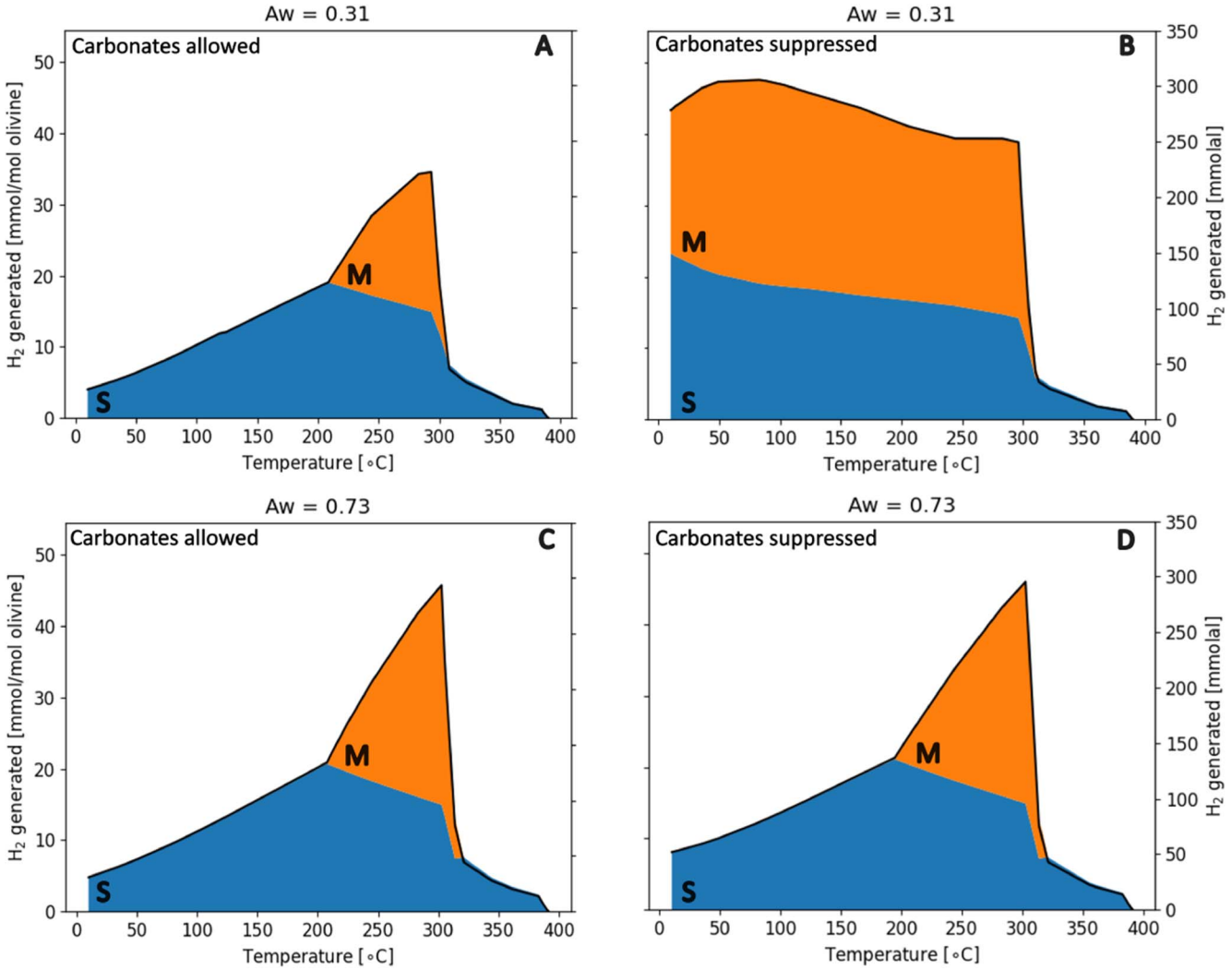

Figure 6. Prediction of H_2 generated based solely on Fe^{3+} in alteration minerals. (A) and (C): Carbonate minerals are allowed to precipitate during serpentinization. (B) and (D): Carbonate mineral formation is suppressed during serpentinization. M: Magnetite contribution to H_2 generation. S: Serpentinite contribution to H_2 generation. (C) and (D) compare favorably to the results of McCollom et al. (2022) (their Figure 4(A)).

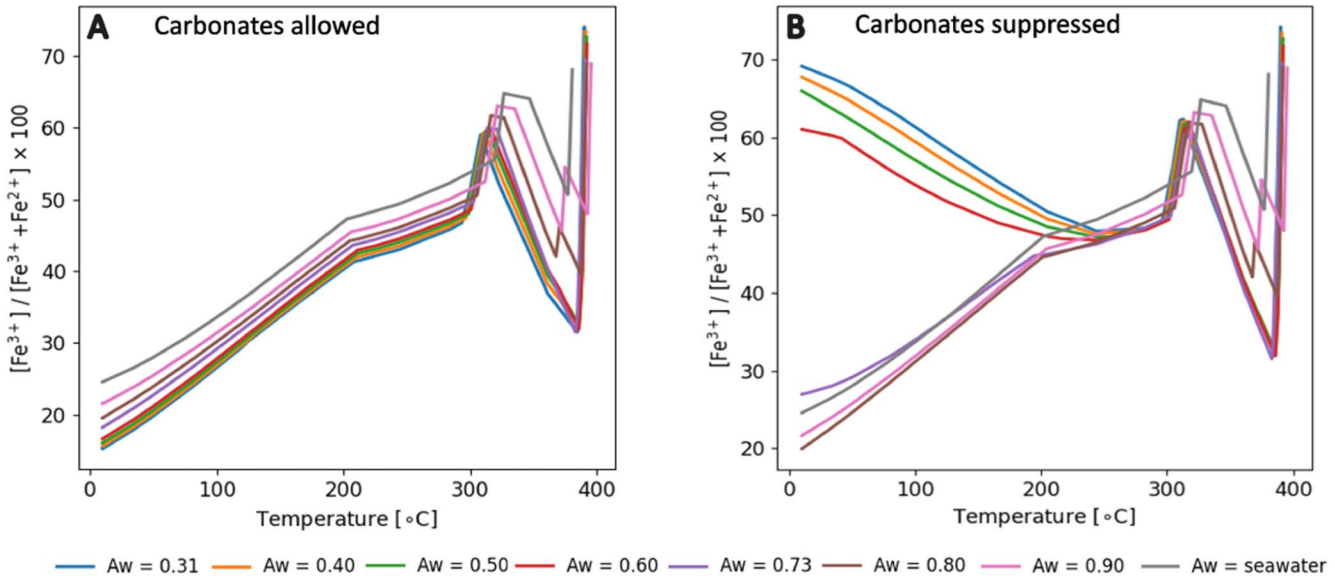

Figure 7. (A) and (B): Ratios of calculated $Fe^{+3}/(Fe^{+3} + Fe^{+2})$ ratios of serpentine solid solution. (A): Carbonate mineral formation is allowed. (B): Carbonate mineral formation is suppressed.

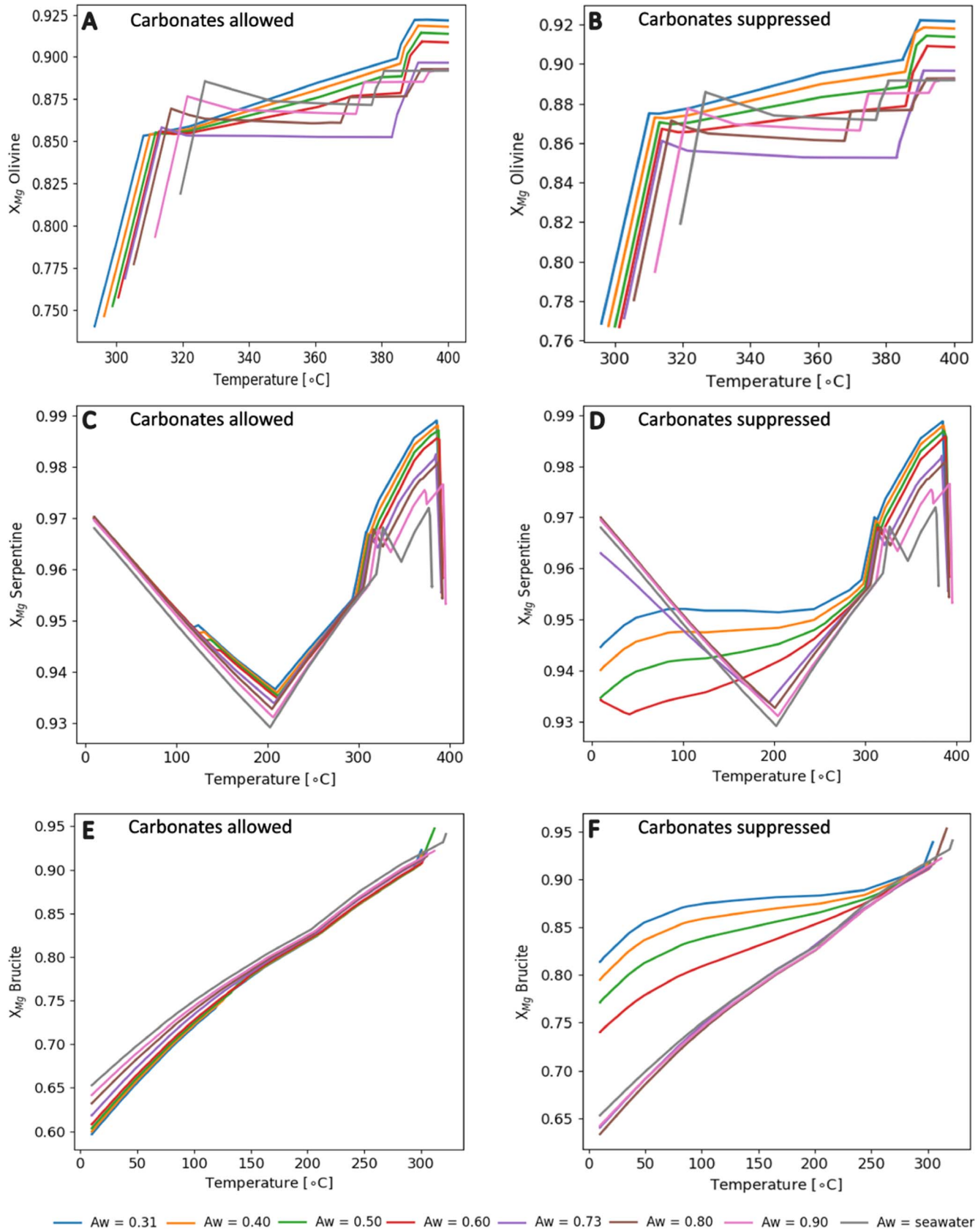

Figure 8. (A) and (B): Fe content (X_{Mg} in the notation of Klein et al. (2013), often reported as Mg#) of olivine solid solution. (C) and (D): Fe content (as X_{Mg}) of serpentine solid solution. (E) and (F): Fe content (as X_{Mg}) of serpentine solid solution. All curves represent water:rock reactions of W:R ∼1. Aw is the water activity of the reacting fluid. (A), (C), and (E): Carbonate mineral formation is allowed during serpentinization. (B), (D), and (F): Mineral carbonate formation is suppressed during serpentinization.

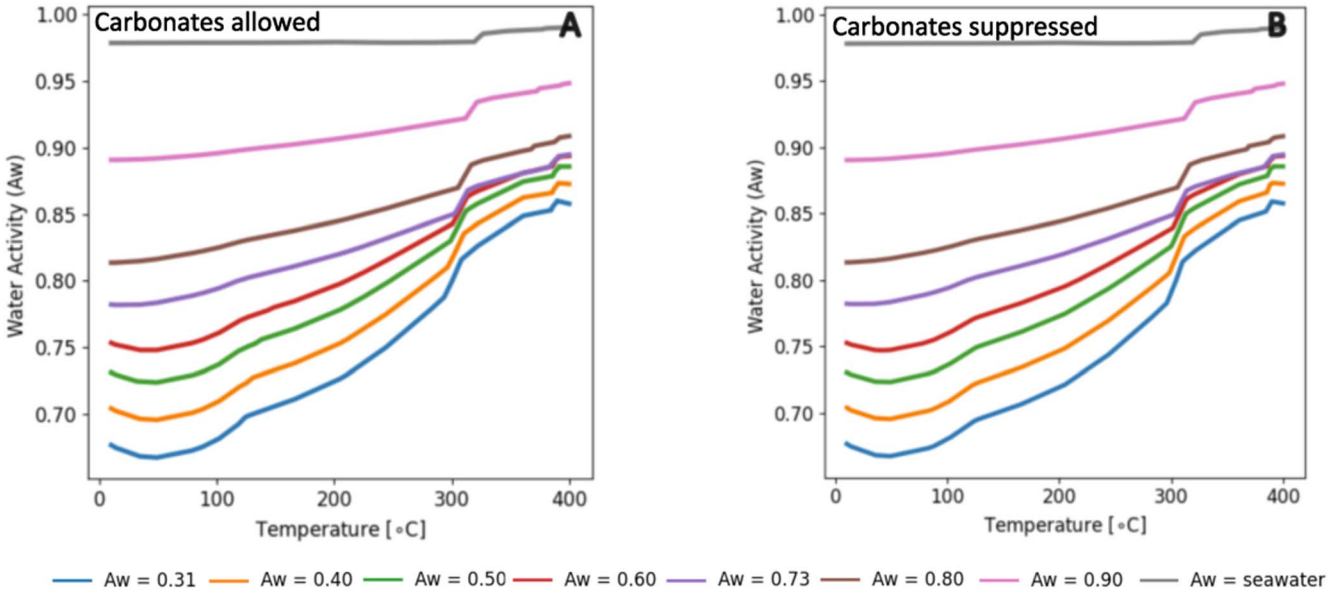

Figure 9. Water activity changes resulting from the serpentinization of distinct brine compositions of varying Aw as a function of temperature at 350 bar (35 MPa) and a water:rock ratio equal to 1. (A): Carbonate mineral formation is allowed. (B): Carbonate mineral formation is suppressed. DIC does not meaningfully alter the water activity of the serpentinized fluid. Caution is advised because these Aw values are computed with a Debye–Hückel approximation for activity coefficients. See text for details.

significantly impacts the extent of iron oxidation and the generation of H_2.

We also predict that the contribution of serpentine and magnetite to H_2 generation during serpentinization with low-Aw fluids is elevated compared to serpentinization with higher Aw fluids (Figure 6) when DIC supersaturation can occur. The iron content of brucite, denoted by the Mg# (or X_{Mg}), can exhibit substantial variations depending on the presence of the $Fe(OH)_2$ component in the solid solution. The Mg# is the molar ratio of Mg to Mg+Fe in a mineral. Although Mg# can range from 0.95 to as low as 0.65 in certain natural samples (e.g., Templeton & Ellison 2020), thermodynamic studies conducted by Klein et al. (2013) demonstrated that it is possible to have brucite with a higher iron content (e.g., Mg# < 0.65) as a result of the serpentinization of ultramafic rocks containing iron-rich olivine with a composition approaching the fayalite endmember. Nevertheless, Figure 8 illustrates that serpentinization with low-Aw fluids results in the formation of brucites with higher Mg# values at lower temperatures when carbonate minerals are prevented from forming. This suggests that, in this scenario, brucite holds less iron, and it becomes more likely that iron undergoes oxidation during the process of serpentinization. This observation is supported by the generation of serpentines with higher iron content (indicated by lower Mg# values) and an increased presence of Fe^{3+} within them, alongside the production of more magnetite occurring at lower temperatures (again when carbonates are prevented from forming; see Figure 7).

The consumption of hydrogen by CO_2 prevents magnetite from altering to Fe-brucite via (Klein et al. 2013)

$$Fe_3O_4 + 2H_2O + H_2 \leftrightarrows 3Fe(OH)_2, \quad (7)$$

and thus magnetite is found in the low-temperature alteration mineralogy (Figure 5(B)). In contrast, formate is not energetically favored when DIC-poor fluids like seawater are the reacting fluids. In these conditions, while some H_2 is consumed via back-reaction with magnetite to form brucite, eliminating magnetite from the low-temperature mineral assemblage (Figures 5(A) and (D)), H_2 can remain in the fluid (Figure 3(B)).

The high-temperature drop in H_2 concentration at $T \sim 320$°C (Figure 3) is due to changes in the stability field of olivine (Figure 5). Indeed, during seawater alteration of harzburgite, olivine alters into secondary phases. It does not persist until high temperatures ($T > \sim$320°C) are achieved. This enables the H_2 concentration to increase up to that temperature. Above ~320°C, the thermodynamic stability of olivine precludes the dissolution of iron in olivine and its subsequent oxidation, causing the resulting H_2 concentrations to drop precipitously given that olivine is the main source of Fe^{2+} in harzburgites. We observe that the salinity of brines expressed as different water activities pushes the stability field of olivine to somewhat lower temperatures. At Aw = 0.31, for example, olivine is stable at $T >$ ~300°C. Only the iron in pyroxene is thus available for oxidation and hydrogen generation above that temperature. The stability field of olivine is pushed toward lower temperatures when brines are the reacting fluid, because of the computational treatment of olivine as a solid solution. We acknowledge that the composition of olivine is best treated as fixed when reacting ultramafic rocks with seawater (McCollom & Bach 2009). Whether this truth applies to systems where brines are dominant is unknown. As a result, we chose not to constrain the composition of olivine in this study. This has minimal effect on hydrogen generation (Figure 3), but it does affect the temperature stability field of olivine slightly. Indeed, Figures 8 (A) and (B) show that the stable high-temperature olivine progressively becomes richer in iron as saltier reacting fluids are used. Pure fayalite, the iron endmember of olivine, is stable at temperatures as low as 180°C (Klein et al. 2013). Increasing the fayalite content in olivine, therefore, depresses the stability temperature.

Water activity increases markedly, independent of starting fluid Aw, during the heating process (Figure 9). Yet, caution in this result is warranted because of the necessary change in the activity coefficient model used for serpentinization (the "B-dot"

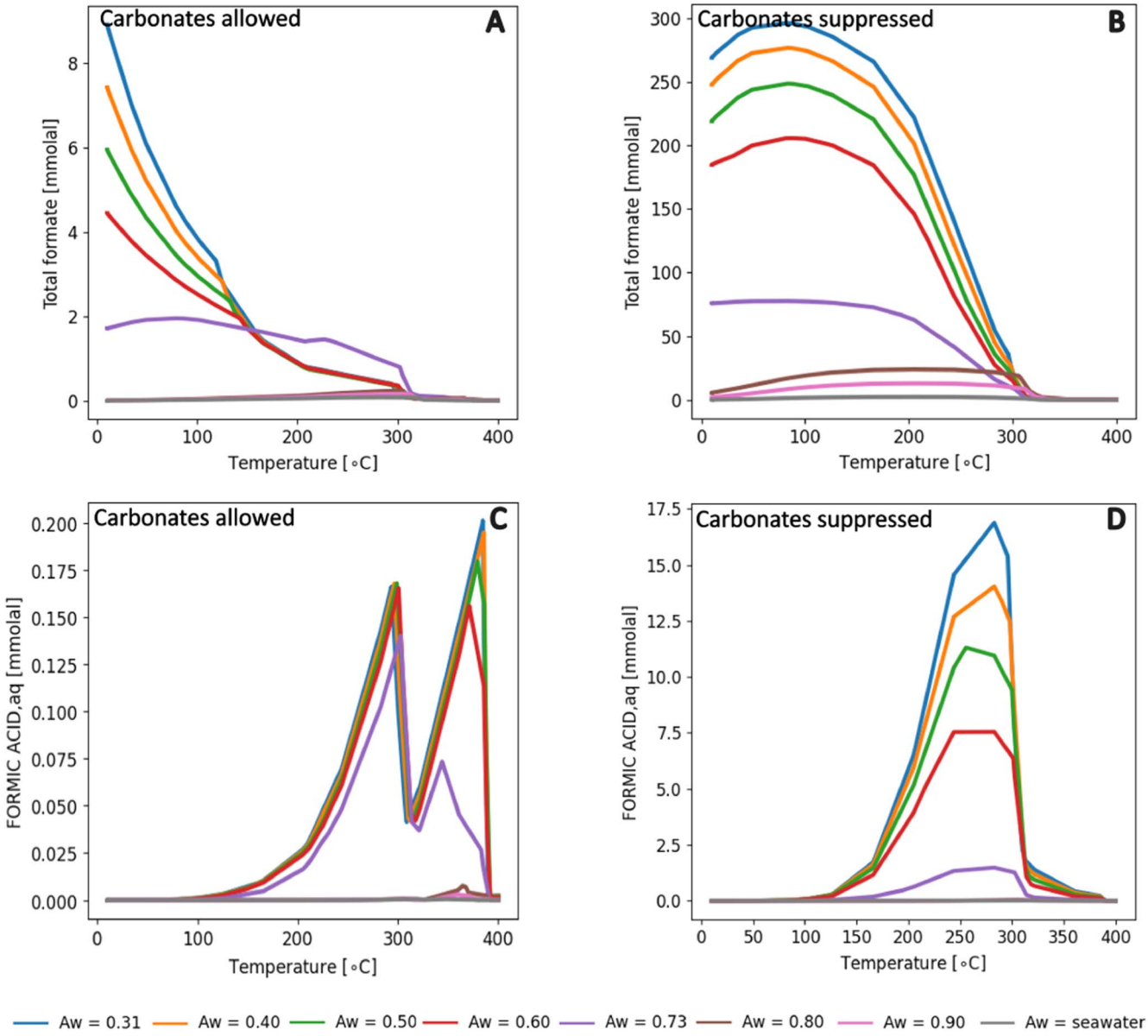

Figure 10. Total formate ((A) and (B)) and formic acid ((C) and (D)) resulting from the serpentinization of distinct brine compositions of varying Aw as a function of temperature at 350 bar (35 MPa) and a water:rock ratio equal to 1. (A): Carbonate mineral formation is allowed. (B): Carbonate mineral formation is suppressed. Note the differences in scale. Total formate is the sum of formate and formate complexes as defined by Equation (6).

extended Debye–Hückel formulation) from that of brine creation (Pitzer equations). The largest errors in the computation of bulk properties like Aw and ionic strength will come from recomputing brine chemistry initially derived with Pitzer equations using Debye–Hückel (D-H) approximations. For example, the briniest fluid ($Aw_{Pitzer} = 0.31$) was recomputed to have a starting $Aw_{D\text{-}H}$ of 0.67. This ΔAw ($Aw_{D\text{-}H} - Aw_{Pitzer}$) decreases the more dilute the starting brine is. As the serpentinized fluid is heated, the water activity increases, consistent with an expected decrease in the ionic strength of the fluid. Whether and at what temperature this increase of Aw crosses the Aw threshold for microbial metabolism ($Aw = 0.540$; Paris et al. 2023) remains unclear, given ΔAw, but it does suggest that, from an Aw perspective, even if the starting fluids are too concentrated in salts to allow for biological processes as we know them, as long as fluids can flow to reactions zones where unaltered rocks exist (e.g., Paukert et al. 2012) and temperatures remain moderate, habitable conditions may be reached.

On Earth, the water:rock ratio varies depending on the reaction setting and contributes to the underlying geochemical dynamics. A low water:rock ratio implies a larger volume of rock is reacting with a smaller volume of water. This generally characterizes on-axis hydrothermal systems where rocks have not undergone significant alteration during hydrothermal activity, and mainly the chemistry of the rock controls the geochemical evolution of the system (Von Damm et al. 1985). A high water:rock ratio implies a smaller amount of rock is reacting with larger volumes of water. This can be seen in off-axis hydrothermal settings where the reacting rock has already been subjected to intense alteration (Coogan & Gillis 2018), and the water composition (and temperature) mainly drives the fate of the equilibrium reaction products. We bracket these hydrothermal settings in Figure 11, illustrating H_2

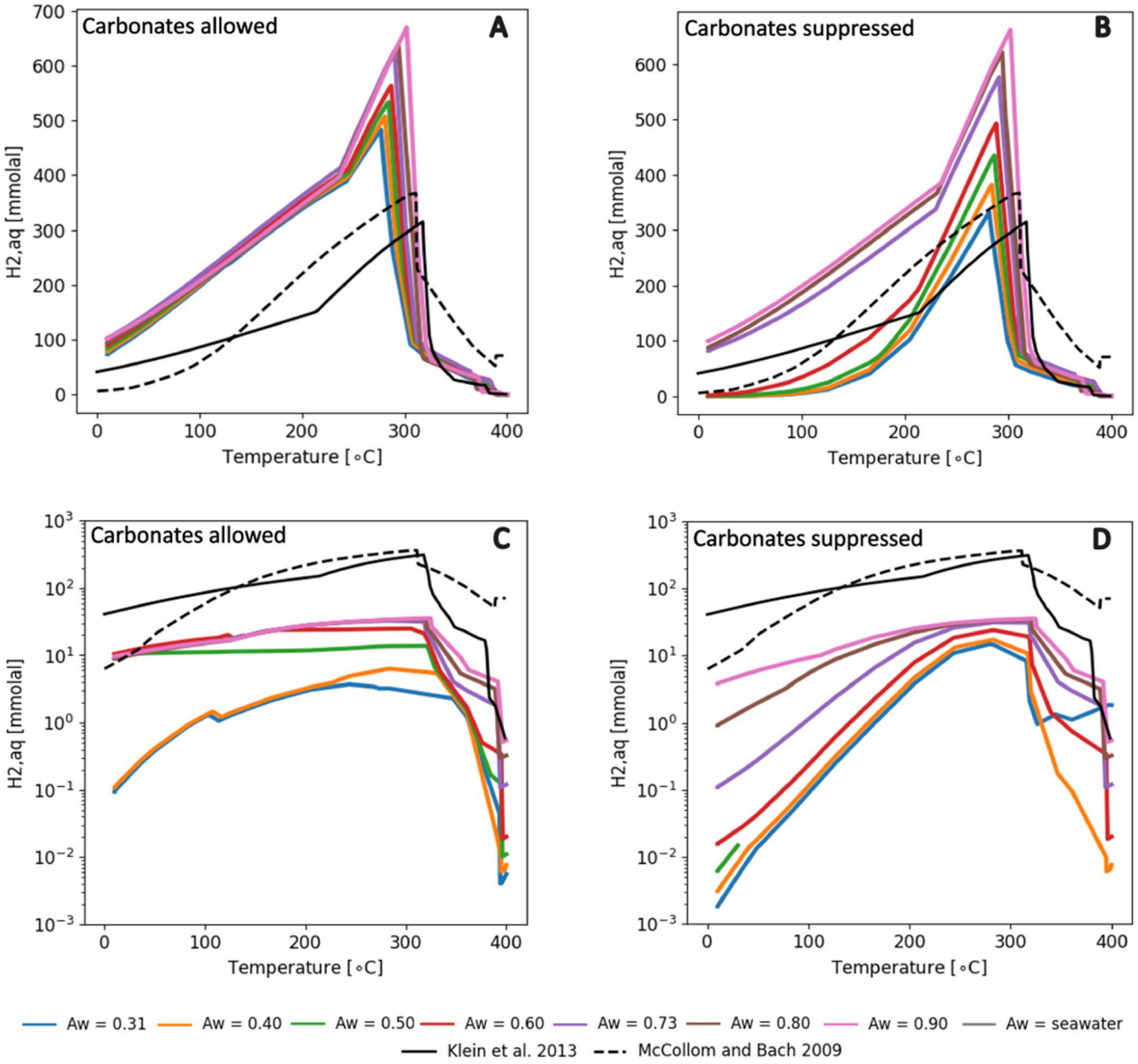

Figure 11. Hydrogen in seawater-derived brines resulting from the serpentinization of distinct brine compositions of varying Aw as a function of temperature at 350 bar. (A) and (B): Water to rock ratio = 0.5. (C) and (D): Water to rock ratio = 10. (A) and (C): Carbonate mineral formation allowed during serpentinization. (B) and (D): Carbonate mineral formation suppressed during serpentinization.

generation at W:R = 0.5 and W:R = 10. At peak H_2 production ($T \sim 300°C$), the difference in H_2 produced is almost a thousandfold. Thus, water:rock ratio is an important variable to constrain for planetary estimates of H_2 production by serpentinization.

Understanding the geochemical controls on the production of hydrogen has ramifications beyond geochemistry. Indeed, hydrogen is an important bioavailable source of energy. Hydrogen is an electron donor that supports chemosynthetic biology in the subsurface (e.g., Hoehler 2005; Templeton & Caro 2023) and plausibly on extraterrestrial bodies (e.g., Schulte et al. 2006; Waite et al. 2017). While most of the effort to date has focused on the lithology as a control on hydrogen generation via iron oxidation (e.g., Ely et al. 2023), we have emphasized in this communication the role of water composition via brines of different water activities derived from evaporation of seawater. This has highlighted the DIC content and pH of the serpentinizing fluid as major controllers of hydrogen concentration in the equilibrium system. An important driver of formate production is CO_2 availability, which DIC speciates to favorably in acidic environments. Both salts and elevated pCO_2 (if waters are exposed to a CO_2-rich atmosphere) can drive pH down. An important driver of DIC content is the extent of carbonate supersaturation, the nucleation kinetics of which are affected by the presence of magnesium ions (Pytkowicz 1965) and dissolved (or soluble) organic matter (Chave & Suess 1970; Jun et al. 2022), the latter adsorbing onto mineral carbonate nuclei and arresting their continued growth.

Such drivers may apply to planetary fluids as well. Martian aqueous fluids, for instance, likely include brines (Martínez & Renno 2013). Sources of organic material on planetary surfaces

are varied (Steele et al. 2016, 2018, 2022) and thus not limited to terrestrial processes alone. For example, organic material has been detected in the plumes of Saturn's moon Enceladus (Postberg et al. 2018; Khawaja et al. 2019). Organic material has also been found to coexist with minerals consistent with aqueous processes on Mars (Sharma et al. 2023), likely due to the contribution of carbonaceous chondrites to the Martian impactor population, and Mars may have hosted DIC-rich acidic fluids in its past (Hurowitz et al. 2023). This makes high-DIC terrestrial fluids useful analogs for early Mars surface waters.

The loss of hydrogen via total formate production could affect life on icy satellites. Indeed, a CO_2-rich early ocean has been proposed for Europa (Melwani Daswani et al. 2021). In icy satellites, in general, the concentration of ions in brine would occur during the freezing of water. Furthermore, carbonaceous chondrites contribute abundantly to the composition of icy satellite interiors (McKinnon & Mueller 1989). Carbonaceous chondrites comprise up to 4 wt.% carbonaceous and organic compounds, 25% of which is soluble carbonaceous matter (Néri et al. 2020). Other likely contributors of organics to icy satellites include comets (Fray et al. 2016), which may also include soluble organic compounds (Mumma & Charnley 2011). These soluble compounds plausibly may cause some DIC supersaturation in non-terrestrial liquid bodies.

5. Conclusions

We simulated the serpentinization of harzburgite with a set of seawater-derived brines of varying water activity as a proxy for salinity. Such salty fluids, derived by evapoconcentration closed to the atmosphere, created brines of increasing DIC and acidity content. In our serpentinization simulation, we bracketed the solution in between two cases. In one case, carbonate mineral formation was suppressed, and in the other, carbonate mineral formation was enabled. We did so to consider the role magnesium ions and organic matter play in supersaturating DIC in a fluid. We found that hydrogen released by the serpentinization of harzburgite with high DIC fluids can react with CO_2 to form formate and formate complexes via reduction. Acidity is enhanced by salinity through the increase, by a factor of 10, of the activity coefficient of H^+ at NaCl saturation. DIC preferentially speciates to CO_2 at lower pH. The limited availability of hydrogen allows magnetite to remain stable, at the expense of brucite formation, down to the lowest temperature of our investigation, 10°C. We also found that brines can affect the thermodynamic stability field of protolith minerals if olivine is treated as a solid solution. Olivine was stable at lower temperatures when altered with brines compared to seawater. Our work indicates that, in addition to the already recognized influence of rock mineralogy and composition, the composition of water, in particular the DIC content and pH, also plays a significant role in controlling the abundance of hydrogen derived from serpentinization.

Acknowledgments

This work was funded as part of the Oceans Across Space and Time program of the NASA Astrobiology Program, grant 80NSSC18K1301, PI B.E. Schmidt. S.M.S. further acknowledges the Exploring Ocean Worlds program of the NASA Astrobiology Program, grant 80NSSC19K1427, PI C. German, for support. This project was completed as part of the BMSIS Young Scientist Program and Visiting Scholar Program by S.S. and A.A.S. under the mentorship of S.M.S. S.M.S. further acknowledges T.M.H., M.J.A., and T.M.M. for mentorship and acknowledges Sunanda Sharma for discussions on planetary organics. We thank Kirt Robinson and the Oceans Across Space and Time team for feedback on improving the manuscript, as well as two reviewers who provided insightful comments that further improved the manuscript's clarity.

ORCID iDs

Sanjoy M. Som https://orcid.org/0000-0001-7684-0151
Serhat Sevgen https://orcid.org/0000-0002-3858-1109
Jeff S. Bowman https://orcid.org/0000-0002-8811-6280
Britney E. Schmidt https://orcid.org/0000-0001-7376-8510

References

Abrajano, T. A., Sturchio, N. C., Bohlke, J. K., et al. 1988, ChGeo, 71, 211
Abrajano, T. A., Sturchio, N. C., Kennedy, B. M., et al. 1990, ApGC, 5, 625
Alt, J. C., Shanks, W. C., Bach, W., et al. 2007, GGG, 8, Q08002
Andersen, G. M. 1996, Thermodynamics of Natural Systems (New York: Wiley)
Antunes, A., Olsson-Francis, K., & McGenity, T. J. 2020, Curr. Issues Mol. Biol., 38, 123
Barnes, I., & O'Neil, J. R. 1969, GSAB, 80, 1947
Barnes, I., O'Neil, J. R., & Trescases, J. J. 1978, GeCoA, 42, 144
Bodinier, J. L., & Godard, M. 2003, TrGeo, 2, 103
Brazelton, W. J., Nelson, B., & Schrenk, M. O. 2012, Front. Microbiol., 2, 268
Buffo, J. J., Schmidt, B. E., Huber, C., et al. 2020, JGRE, 125, e06394
Castillo-Rogez, J., Weiss, B., Beddingfield, C., et al. 2023, JGRE, 128, e2022JE007432
Charlou, J. L., Donval, J. P., Fouquet, Y., et al. 2002, ChGeo, 191, 345
Chave, K. E., & Suess, E. 1970, LimOc, 15, 633
Colman, D. R., Kraus, E. A., Thieringer, P. H., et al. 2022, PNAS, 119, e2206845119
Coogan, L. A., & Gillis, K. M. 2018, AREPS, 46, 21
Douville, E., Charlou, J. L., Oelkers, E. H., et al. 2002, ChGeo, 184, 37
Duan, Z., & Sun, R. 2003, ChGeo, 193, 257
Ehlmann, B. L., Mustard, J. F., & Murchie, S. L. 2010, GeoRL, 37, L06201
Ejeian, M., Grant, A., Shon, H. K., & Razmjou, A. 2021, Desal, 518, 115169
Ely, T. D., Leong, J. M., Canovas, P. A., et al. 2023, GGG, 24, e2022GC010658
Etiope, G., Schoell, M., & Hosgörmez, H. 2011, E&PSL, 310, 96
Evans, B. W. 2004, IGRv, 46, 479
Evans, B. W., Hattori, K., & Baronnet, A. 2013, Elements, 9, 99
Fisher, L. A., Pontefract, A., Som, S. M., et al. 2021, EnvMi, 23, 3360
Fray, N., Bardyn, A., Cottin, H., et al. 2016, Natur, 538, 72
Frost, B. R., & Beard, J. S. 2007, JPet, 48, 1351
German, C. R., Reeves, E. P., Türke, A., et al. 2022, NatCo, 13, 6517
Glein, C. R., Baross, J. A., & Waite, J. H., Jr 2015, GeCoA, 162, 202
Glein, C. R., Postberg, F., & Vance, S. D. 2018, in Enceladus and the Icy Moons of Saturn, ed. P. M. Schenk et al. (Tucson, AZ: Univ. Arizona Press), 39
Grozeva, N. G., Klein, F., Seewald, J. S., et al. 2020, RSPTA, 378, 20180431
Hamilton, V. E., Christensen, P. R., McSween, H. Y., & Bandfield, J. L. 2003, M&PS, 38, 871
Hand, K. P., Bartlett, D. H., Fryer, P., et al. 2020, DSRI, 160, 103238
Helgeson, H. C. 1969, AmJS, 267, 729
Hoehler, T. M. 2005, in Metal Ions in Biological Systems, Vol. 43—Biogeochemical Cycles of Elements, ed. A. Sigel, H. Sigel, & R. K. O. Sigel (1st ed.; Boca Raton, FL: CRC Press), 9
Holm, N. G., Oze, C., Mousis, O., et al. 2015, AsBio, 15, 587
Hosgormez, H., Etiope, G., & Yalçin, M. N. 2008, Gflui, 8, 263
Howells, A. E., Leong, J. A., Ely, T., et al. 2022, JGRG, 127, e2021JG006317
Huang, R., Shang, X., Zhao, Y., Sun, W., & Liu, X. 2023, JGRB, 128, e2022JB025218
Hurowitz, J. A., Catling, D. C., & Fischer, W. W. 2023, Elements, 19, 37
Jones, L. C., Rosenbauer, R., Goldsmith, J. I., & Oze, C. 2010, GeoRL, 37, L14306
Jun, Y. S., Zhu, Y., Wang, Y., et al. 2022, ARPC, 73, 453
Kelley, D. S., Karson, J. A., Blackman, D. K., et al. 2001, Natur, 412, 145

Kelley, D. S., Karson, J. A., Fruh-Green, G. L., et al. 2005, Sci, 307, 1428
Kelley, D. S., & Shank, T. M. 2010, GMS, 188, 369
Khawaja, N., Postberg, F., Hillier, J., et al. 2019, MNRAS, 489, 5231
Klein, F., Bach, W., Jöns, N., et al. 2009, GeCoA, 73, 6868
Klein, F., Bach, W., & McCollom, T. M. 2013, Litho, 178, 55
Klempay, B., Arandia-Gorostidi, N., Dekas, A. E., et al. 2021, EnvMi, 23, 3825
Koepke, J., Seidel, E., & Kreuzer, H. 2002, Litho, 65, 183
Lamadrid, H. M., Rimstidt, J. D., Schwarzenbach, E. M., et al. 2017, NatCo, 8, 16107
Leong, J. A. M., & Shock, E. L. 2020, AmJS, 320, 185
Liu, C., Lowenstein, T. K., Wang, A., et al. 2023, Annu. Rev. Environ. Resour., 48, 371
Long, D. T., & Angino, E. E. 1977, GeCoA, 41, 1183
Lugli, S., Manzi, V., Roveri, M., et al. 2015, PPP, 433, 201
Malamud, U., & Prialnik, D. 2013, Icar, 225, 763
Martin, W., & Russell, M. J. 2007, RSPTB, 362, 1887
Martínez, G., & Renno, N. O. 2013, SSRv, 175, 29
Mayhew, L. E., Ellison, E. T., McCollom, T. M., et al. 2013, NatGe, 6, 478
Mayhew, L. E., Ellison, E. T., Miller, H. M., Kelemen, P. .B, & Templeton, A. T. 2018, GeCoA, 222, 704
McCaffrey, M. A., Lazar, B. H. D. H., & Holland, H. D. 1987, JSedR, 57, 928
McCollom, T. M. 2016, PNAS, 113, 13965
McCollom, T. M., & Bach, W. 2009, GeCoA, 73, 856
McCollom, T. M., Klein, F., & Ramba, M. 2022, Icar, 372, 114754
McCollom, T. M., Klein, F., Robbins, M., et al. 2016, GeCoA, 181, 175
McCollom, T. M., Klein, F., Solheid, P., & Moskowitz, B. 2020, RSPTA, 378, 20180428
McCollom, T. M., & Seewald, J. S. 2001, GeCoA, 65, 3769
McCollom, T. M., & Seewald, J. S. 2003, GeCoA, 67, 3625
McCollom, T. M., & Seewald, J. S. 2013, Elements, 9, 129
McDermott, J. M. 2015, PhD thesis, MIT
McKinnon, W. B., & Mueller, S. 1989, GeoRL, 16, 591
Melwani Daswani, M. M., Vance, S. D., Mayne, M. J., et al. 2021, GeoRL, 48, e94143
Millero, F. J. 2009, Chemical Oceanography (Boca Raton, FL: CRC Press)
Moody, J. B. 1976, Litho, 9, 125
Mumma, M. J., & Charnley, S. B. 2011, ARA&A, 49, 471
Néri, A., Guyot, F., Reynard, B., & Sotin, C. 2020, E&PSL, 530, 115920
Nordstrom, D. K., Plummer, L. N., Wigley, T. M. L., et al. 1979, in Chemical Modeling in Aqueous Systems, ed. E. A. Jenne (Washington, DC: American Chemical Society), 857
Oelkers, E. H., Declercq, J., Saldi, G. D., et al. 2018, ChGeo, 500, 1
Olsen, A. A., Hausrath, E. M., & Rimstidt, J. D. 2015, JGRE, 120, 388
Palandri, James L, & Reed, Mark H 2004, GeCoA, 68, 1115
Paris, E. R., Arandia-Gorostidi, N., Klempay, B., et al. 2023, SciA, 9, eadj3594
Paukert, A. N., Matter, J. M., Kelemen, P. B., et al. 2012, ChGeo, 330, 86
Pitzer, K. S. 1973, JPCA, 77, 268
Pitzer, K. S., Peiper, J. C., & Busey, R. H. 1984, JPCRD, 13, 1
Pokrovsky, O. S., & Schott, J. 2000, GeCoA, 64, 3313
Postberg, F., Khawaja, N., Abel, B., et al. 2018, Natur, 558, 564
Pytkowicz, R. M. 1965, J. Geol., 73, 196
Rempfert, K. R., Miller, H. M., Bompard, N., et al. 2017, Front. Microbiol., 8, 56
Rivera-Valentín, E. G., Chevrier, V. F., Soto, A., & Martínez, G. 2020, NatAs, 4, 756
Russell, M. J., Hall, A. J., & Martin, W. 2010, Gbio, 8, 355
Samylina, O. S., Sapozhnikov, F. V., Gainanova, O. Y., et al. 2014, Microbiology, 83, 849
Schmidt, K., Koschinsky, A., Garbe-Schönberg, D., et al. 2007, ChGeo, 242, 1
Schmidt, K., Garbe-Schönberg, D., Koschinsky, A., Strauss, H., Jost, C.L., Klevenz, V., & Königer, P. 2011, ChGeo, 280, 1
Schuiling, R. D. 2011, IJG, 2, 98
Schulte, M., Blake, D., Hoehler, T., & McCollom, T. 2006, AsBio, 6, 364
Scully, J. E. C., Schenk, P. M., Castillo-Rogez, J. C., et al. 2020, NatCo, 11, 3680
Seyfried, W. E., Jr, Foustoukos, D. I., & Fu, Q. 2007, GeCoA, 71, 3872
Seyfried, W. E., Jr, Pester, N. J., Ding, K., & Rough, M. 2011, GeCoA, 75, 1574
Seyfried, W. E., Jr, Pester, N. J., Tutolo, B. M., & Ding, K. 2015, GeCoA, 163, 59
Sharma, S., Roppel, R. D., Murphy, A. E., et al. 2023, Natur, 619, 724
Sherwood Lollar, B., Voglesonger, K., Lin, L. H., et al. 2007, AsBio, 7, 971
Som, S., Sevgen, S., & Suttle, A., 2024 The chEQWRk v0.1.0 code, NASA Ames AHED, doi:10.48667/rbvs-df39
Sonzogni, Y., Treiman, A. H., & Schwenzer, S. P. 2017, JMPeS, 112, 59
Spycher, N., & Pruess, K. 2005, GeCoA, 69, 3309
Steele, A., Benning, L. G., Wirth, R., et al. 2018, SciA, 4, eaat5118
Steele, A., Benning, L. G., Wirth, R., et al. 2022, Sci, 375, 172
Steele, A., McCubbin, F. M., & Fries, M. D. 2016, M&PS, 51, 2203
Stevenson, A., Hamill, P. G., O'Kane, C. J., et al. 2017, EnvMi, 19, 687
Templeton, A. S., & Caro, T. A. 2023, AREPS, 51, 493
Templeton, A. S., & Ellison, E. T. 2020, RSPTA, 378, 20180423
Tutolo, B. M., & Tosca, N. J. 2023, SciA, 9, eadd8472
Vitale Brovarone, A., Martinez, I., Elmaleh, A., et al. 2017, NatCo, 8, 14134
Vitale Brovarone, A., Sverjensky, D. A., Piccoli, F., et al. 2020, NatCo, 11, 3880
Von Damm, K. L, Edmond, J. M, Grant, B., et al. 1985, GeCoA, 49, 2197
Waite, J. H., Glein, C. R., Perryman, R. S., et al. 2017, Sci, 356, 155
Weiss, B. P., Biersteker, J. B., Colicci, V., et al. 2021, GeoRL, 48, e2021GL094758
Wolery, T. J. 1990, AmJS, 290, 296
Wolery, T. J. 2013, EQ3/6 - Software for Geochemical Modeling, Version 8.0a. LLNL-CODE-2013-683958, Lawrence Livermore Natl. Laboratory
Wolery, T. J., & Jarek, R. L. 2003, Software User's Manual EQ3/6, Version 8.0, Sandia National Laboratories
Wolery, T. W., & Jove-Colon, C. F. 2004, Qualification of Thermodynamic Data for Geochemical Modeling of Mineral-Water Interactions in Dilute Systems ANL-WIS-GS-000003 REV 00, Bechtel SAIC Company, LLC
Zandanel, A., Hellmann, R., Truche, L., et al. 2022, NatAs, 6, 554
Zolotov, M. Y., & Kargel, J. S. 2009, in Europa, ed. R. T. Pappalardo, W. B. McKinnon, & K. Khurana (Tucson, AZ: Univ. Arizona Press), 431